Monitoring water quality in the Lower Kansas River using remote sensing

Nicholas Tufillaro, Philipp Grötsch, Ivan Lalović,
Sara De Moitié, Luke Zeitlin, Omar Zurita
Gybe, Portland, OR
(Correspondence Author: nick@gybe.eco)

June 11, 2024

Abstract

We demonstrate how to combine remote sensing data from satellite imagery (Sentinel-2) with *in situ* water quality gauging (USGS Super Gage's and the Gybe hyperspectral radiometer) to create spatially dense maps of water quality parameters (chlorophyll-a concentration, turbidity, and nitrate plus nitride concentration) along the Lower Kansas River. The water quality maps are created using locally tuned models of the target water quality parameters, and this study describes the steps used to design, calibrate, and validate the empirical correlations. Water quality parameters such as chlorophyll-a concentration are correlated to well-studied absorption and scattering features in the visible spectrum (roughly 400-700 nm). Nutrients (such as nitrate plus nitride concentration) typically lack strong absorption features in the visible spectrum, and in those cases we describe a novel surrogate data modeling approach that identifies overlapping water parcels between the *in situ* gauging and the remote sensing imagery. Measurements from the overlapping water parcels yield excellent correlations ($R^2 > 0.9$) for the target water quality parameters for limited windows of time (or limited sections of river reaches). Examples are provided illustrating how the water quality maps can be used to track river inputs from unguaged sources (such as creeks), or the mixing patterns at river and creek confluences.

Keywords

Kansas River, water quality, remote sensing, nitrates, nutrients, turbidity, harmful algal blooms, hyperspectral.

1 Introduction

The Lower Kansas River is located in northeastern Kansas. It runs from just west of Lecompton, KS, to the confluence of the Kansas River with the Missouri River in Kansas City, MO. The Lower Kansas River Watershed is an agricultural region (pasture/hay and croplands) with significant population centers (Lawrence, KS, population ∼100,000) [1]. The Kansas river control structures are managed for multiple goals ranging from flood control, irrigation needs, drinking water supplies, and environmental flows [2]. The Lower Kansas River water quality is impacted by storm runoff, which can carry significant sediment loads that transport nutrients (nitrate, phosphate), bacteria (e-coli), metals (Pb, Cu), and other products from natural and man-made activities [3].

The Kansas River is an ecologically impaired river system. Its restoration and protection is a high priority for state and national agencies. A diverse set of stakeholders from local community groups (e.g., Friends of the KAW [4]) to NGOs (e.g., The Nature Conservancy [5]) are actively involved in restoration and ecological management efforts. A key component of all these activities is gauging the water quality. To achieve adequate temporal coverage, the USGS maintains high frequency (15-minute sampling) Super Gage's providing water quality parameters such as chlorophyl-a concentrations, turbidity, and some nutrients (nitrate) [6]. However, adequate spatial coverage is lacking, which is particularly important in the Kansas River watershed since storm runoff has an important and complex (temporally and spatially) impact on water quality.

This paper looks at how recent satellite imagery with high spatial resolution, in particular, the European space agencies constellation known as Sentinel-2 (10-meter nominal spatial resolution) [7] can provide water quality maps with dense spatial coverage along the Kansas River. Starting from publicly available satellite data, we give an account of how to generate water quality products such as turbidity, chlorophyll-a concentrations and nitrate plus nitrite concentrations. We then present examples of remote sensing imagery revealing the patterns formed by the water constituents along the Kansas river.

The absorption of electromagnetic radiation by water is relatively low across the visible spectrum (∼300–700 nm). This makes the (above-water) remote detection of target parameters, such as like chlorophyll-a concentrations or turbidity, relatively easy because they posses robust signatures across the visible spectrum. Conversely, the detection of target variables, such as nitrate with features outside the visible spectrum (absorption ∼220 nm [8]), are more problematic. In those cases, surrogate data methods are often utilized to estimate water quality parameters [9].

The standard method for constructing water quality maps from remote sensing imagery correlates historical times series of *in situ* data, such as in water gauges for chlorophyll-a concentrations or turbidity, with reflectance data available from satellite imagery [10]. In this study we report two different techniques intended to improve upon the precision of the water quality maps build using only the standard method. Though distinct, both techniques have a common theme, they attempt to adjust the empirical correlations with contemporaneous *in situ* data, either from in-water gauges or from above-water ground-based reflectance measurements.

The latter technique uses a ground-based hyperspectral radiometer [11, 12] operated as a fiducial reference (co-located with a USGS gaging station) to assist with the atmospheric correction process in deriving water quality product maps from Sentinel-2 imagery. In this effort, we use contemporaneous spectral measurements to reduce the uncertainly in the atmospheric correction. The former technique uses the in-water gauges to construct surrogate models that replace the historical data training set with training data that is contemporaneous to both the satellite imagery and in-water gauges. Both techniques are simple attempts to fuse *in-situ* data with satellite imagery in an effort to provide better estimations of water quality maps.

This paper is organized as follows. Section 2 (Methods) is the most extensive part of the paper and provides a detailed account of the methods used to derive the water quality product maps. The algorithms described are optimized both in their model structure and calibration for the Kansas River site data. Although site-specific, the model selection and calibration process is reproducible for other medium-sized rivers and watersheds with access to high-frequency *in situ* water quality gauges. Section 3 (Results) examines three examples of how the dense spatial information enabled by remote sensing can provide insights into either the gauging or the biogeochemical dynamics affecting water quality processes, particularly during storm runoff events. Section 4 (Discussion) highlights lessons learned and suggests additional research or operational water quality efforts.

2 Methods

We begin with an overview of the sites and data sources used in this study. This is followed by a detailed description of the models we developed for empirical correlations between USGS based *in situ* measurements of water quality and the multispectral Sentinel-2 imagery.

2.1 Sites and Data Sets

The Kansas River (the 'Kaw') flows West to East from Junction City, KS, into the Missouri River at Kansas City, MO. This paper looks at the stretch of river from Mill Creek, west of Topeka, to Randolph, MO, seven river miles east of the confluence of the Kansas and Missouri Rivers. In particular, we focus on the reach from Lawrence, KS, to Kansas City, MO, because of the availability of high-frequency water quality data from a USGS Super Gage in the center of this river section. Three data sources were used in this study: remote sensing satellite imagery from Sentinel-2, high-frequency data from USGS river gauges, and spectroscopic data from an autonomous radiometer – the Gybe sensor.

2.1.1 Satellite imagery

Sentinel-2(A,B) imagery was acquired from ESA's Copernicus Browser, which provides a complete image of the Lower Kansas River every 5-days (Sentinel-2 Tiles T15STD and T15SUD) at nominal spatial resolution of 10 (bands 3, 4) and 20 (band 5) meters. The only USGS Super Gage in this region that includes *in situ* measurements of nitrate plus nitride is located on the bridge at De Soto, KS, and is the central station used for water quality model calibrations in this study. The De Soto station is located at a 'double overpass' for Sentinel-2, so imagery data is available, on average, every 2.5 days at a nominal overpass time of 11:15 CST. The USGS gauging stations used in this study are described in Table 1 and other locations of interest are listed in Table 2.

Sentinel-2 (S2) top-of-atmosphere reflectances (L1C) were processed using Acolite [13] to Remote Sensing Reflectances (Rrs) for correlations to *in situ* water quality parameters and ground-based radiometric measurements. Imagery for locations of interest was further screened by process flagging (e.g., negative reflectance values) and visual inspections. Two data sets were assembled that contained clear imagery for further study: (1) 162 images covering the period from January 2018 to December 2023, and (2) 13 images from 28 July 2021 till 30 October 2021. The latter S2 data set overlaps with the period when data was available from the Gybe sensor, a ground-based spectral radiometer.

2.1.2 De Soto, Kansas: Study area and high-frequency data

The USGS station at De Soto, Kansas (Station ID: 06892350) is approximately 20 miles downstream from Lawrence, KS, and has a large set of *in situ* water quality sensors, including turbidity, chlorophyll-a, and nitrate plus nitride ($NO_3 + NO_2$) dating back to 2014 and earlier. The site is centrally located in a midwest agriculture region. It is a conduit for nitrate from the midwest, traveling eventually to the Mississippi River and the Gulf of Mexico. It exhibits a wide range of nitrate levels from 0.1 to 10 mg/L, usually peaking during spring when fertilizer is first applied to plowed agricultural fields. Sensor measurements from USGS gauges are reported every 15 minutes. We examined data from 2018 to 2023, which had discharges in the range of 10^3 to 10^5 ft^3/s, turbidity between 0-1500 FNU, chlorophyll-a concentrations (as indicated by the corresponding fluorescence line heights) of 0-30 RFU, and nitrate plus nitride concentrations between 0-7 mg/L. For correlations, satellite imagery and surface radiometric data sets were matched to their corresponding USGS data set to within a 15-minute window centered at 11:15 CST.

2.1.3 Hyperspectral data

An autonomous hyperspectral radiometer manufactured by Gybe [11] was installed directly above the USGS gauges on the bridge above the Kansas River at De Soto, KS, as shown in Figure 1. The Gybe sensor measures downwelling irradiance and upwelling surface radiance and is oriented to facilitate matchups with satellite imagery. The De Soto bridge spans the river North to South. This allowed us to point the sensor from the bridge's east side toward the middle of the Kansas River at an azimuth angle of approximately 45 degrees, i.e., North East. The sensor further points 40 degrees from nadir, in alignment with the NASA above-water ocean color radiometric field measurement protocols when the solar angle is at high noon [14].

The Gybe sensor measures light from ∼400-900 nm with ∼10 nm spectral resolution every 5 seconds. Actual sampling integration times range from 100 microseconds to 2 seconds, and data is temporally averaged. The integration time varies with light conditions. During processing the spectra are interpolated to a 1 nm grid (upsampled), so the wavelength grid for the analyzed spectra is $\lambda_k = \{400, 401, 402, ..., 877, 878, 879\}$ nm.

The radiometer was operational from 28 July till 27 October 2021. Data was collected daily from 10 AM to 4 PM CDT and averaged into 3-minute buckets. Reflectance spectra were derived from *downwelling irradiance*, E_d, and *total radiance*, L_t. The total radiance measurement contains both a water surface reflection (so-called *sky-glint* and *sun-glint*, which result from the diffuse reflection of the sky and the sun disc on the water, respectively) and a *water-leaving radiance component*, L_w, that carries the light that has interacted with the water [15] . An estimation of both glint components was computed using a spectral optimization algorithm described in [15] which enables retrieval of water reflectance spectra under a wide range of solar and view angles [16]. The glint was subtracted from surface reflectance, resulting in an estimate for the remote sensing reflectance Rrs [[16], eq. (1)],

$$Rrs = \frac{1}{E_d}\left(L_t - L_{refl}\right) = \frac{L_w}{E_d}. \tag{1}$$

Automated routines like those described in [16] were also applied to gauge the quality of the retrieved spectra based on a range of variability and spectral metrics. Poor signals (due to poor environmental or viewing conditions, rain, cloud shadows, ...) were filtered from the data set. Resulting quality-controlled Rrs spectra were used to estimate correlations to the target water quality parameters, i.e. chlorophyll-a concentration and turbidity.

In part to ensure the data was also temporally decorrelated (and in part in anticipation of a study on satellite match-ups, and to ensure more consistent solar illumination conditions), only one measurement a day was used to match the USGS data sets. In particular, the time for matching was chosen to agree with the Sentinel-2 overpass time at approximately 11:15 AM CST. After processing and filtering, the resulting 'daily' data contained 43 spectra, which were further divided into two categories – a training set of 25 spectra (coincident with days an S2 overpass occurred) and a remaining 'test set' of 18 spectra (on days with no overpass). The test and training set designations were used in studies examining the out-of-sample performance of the water quality correlations.

Despite the limited time frame, a wide range of water conditions were captured in the late summer and fall of 2021. As indicated by USGS gauging, approximately four periods of elevated turbidity occurred (> 100 FNU related to storm runoff) and four periods of elevated chlorophyll-a levels (> 18 RFU) with relatively rapid oscillations between the high turbidity and elevated chlorophyll-a states as described in [17].

The difference between these two distinct water quality states was easy to see in the satellite imagery and the spectra captured by the Gybe sensor. Figure 2(a) shows a Sentinel-2 image of a warm, sunny day in August with deep green water and elevated chlorophyll-a concentrations. The corresponding spectra are shown in Figure 2(b) where a peak at about $\sim$570 nm is easily identified, as well as peaks from red-edge effects [18], and backscatter at $\sim$700nm and $\sim$800nm. The image and spectra in Figure 2 presented a sharp contrast with those in Figure 3, a sunny, high-turbidity day in September. Figure 3(a) shows very brown water, which is also relatively bright due to the high backscatter. Correspondingly, in (Fig. 3(b)) the central peak is now at 700 nm, and the amplitude of the spectra generally increases between 500-700nm since the strong backscatter outweighs water absorption, especially between 650-700nm. One advantage of hyperspectral data is that it allows us to use features with a wide bandwidth in developing a water quality product algorithm – features that may be unique to a specific body of water or a particular water type. Indeed, in this data set, in addition to the absorption features, the overall reflectance slope between 600-700nm is the most prominent feature available to describe the optical (and corresponding water quality) state of the Kansas River as it oscillates between states of high turbidity and high-chlorophyll-a concentrations.

2.2 Correlation and surrogate models of water quality

The next subsections describe the methods we used to create empirical models for water quality target products (turbidity, chlorophyl-a, and nutrient concentrations) from reflectance spectra. Our model development process had three steps – first, we experimented with different single band [19], band ratio [20], and band difference [21] algorithms to identify models with the best correlations; second we calibrated the selected models against the *in situ* and spectral data from the De Soto, KS (USGS 06892350) sensors and; third, we validated the models with water quality sensors downstream from De Soto, specifically the USGS gauges at Lake Quivira (USGS 06892518) and Randolph (USGS 06893060).

One novel aspect of this study, which presents a bit of a detour in the following subsections, is the description of the use of the above water spectral radiometer in order to provide day-to-day vicarious corrections to the atmospheric processing. The remotely sensed reflectances estimated from Sentinel-2 are affected by uncertainties in atmospheric correction. Typically, the largest source of uncertainty stems from the aerosol type and optical depth determination, but other factors such as adjacency effects and glint also come into play. The optical depth of different aerosols are known to potentially vary significantly throughout a day, and from day-to-day [22], however, in many situations they can be assumed fairly uniform across an individual image. Based on the assumption of spatial homogeneity of aerosol optical properties, we attempt a post-correction, computed from fiducial spectral reference matchups, across all the pixels in an image. In evaluating the utility of the fiducial correction we work with the subset of 13 images from the Fall 2021 which have both satellite and *in situ* observations.

After the detour into the use of a fiducial spectral reference, we present the correlations models calibrated with the full data set (162 images) of satellite reflectances (without fiducial corrections) which are used for the results displayed in Section 3.

2.2.1 Turbidity models

We began the modeling process by comparing corresponding S2 and Gybe spectra for the field data collected in the Fall of 2021. Figures 2 and 3 were typical of the shape of the spectra observed for both low and high turbidity waters. Generally, the 'shape' of the spectra between the Gybe and S2 spectra were in reasonable correspondence for wavelengths <= 705 nm, but the spectra systematically differed in two ways. First, reflectances in the deep red and near-IR (>705 nm) were always higher for the S2 bands than the corresponding Gybe bands. This can be explained by the 'adjacency' effects [23, 24]. Second, from scene to scene, an offset between the two spectra was often observed. As mentioned, we hypothesize that the fluctuations in the baseline of the spectra are due, in part, to effects not accounted for adequately in the atmospheric correction, which could include daily variations in continental aerosols, seasonal variations in land cover impacting the adjacency effects, daily environmental variations not detected by flagging (mist, fog, clouds, cloud shadows), illumination and view variations and uncertainties in their correction (e.g., the accuracy of sky glint estimation).

The fluctuations were particularly troublesome for single-band algorithms. We initially tried single-band algorithms for correlating turbidity using forms described by Dogolitti [19] and Nechad [25] (which are produced as part of the standard Acolite processing) and observed that neither algorithm produced useful correlations at the De Soto site, as indicated by coefficient of determination ($R^2 < 0.3$). As an obvious next step, we experimented with band ratio algorithms. As illustrated in Figure 4, an examination of both the Gybe and S2 spectra indicated that the change in slope between S2 band B3 (560 nm) and S2 band B4 (665 nm) was systemically correlated to the turbidity level. The physical basis for this correlation is that the absorption of water increases sharply when approaching the red end of the visible spectrum, however this water absorption effect is muted as backscatter (and turbidity) increases, resulting (absent of other effects) in an increase of the slope between the Sentinel-2 B3 and B4 bands [26].

Figure 5(a) shows a plot of USGS turbidity values and the band ratios of Sentinel-2 bands formed by B3/B3 (i.e., $R_{rs}(560)/R_{rs}(665)$) for the 2018-2023 S2 image set. The data set appeared to be separated into two clusters — normal turbidity events which can be approximately delineated by turbidity values less than ∼200 FNU (and $R_{rs}(560)/R_{rs}(665) > 0.74$) and extreme turbidity events with turbidity values greater than ∼200 FNU (and $R_{rs}(560)/R_{rs}(665) < 0.74$). The lack of correlation for the extreme events is probably due to signal compression and the limited dynamic range in the sensor itself, which is unable to detect changes in reflectance values in the red band due to the extremely high turbidites and associated suspended matter concentrations. We are investigating the use of alternative longer wavelength bands to build useful correlations at higher turbidity levels, but their lower spatial resolution typically limits the the utility of these longer wavelength bands in a river monitoring context [19].

The curvature in the band ratio plot Figure 5(a) suggested utilizing a non-linear polynomial form in our empirical correlation function. Limiting our S2 2018-2023 data set to band ratios $R_{rs}(560)/R_{rs}(665) > 0.74$ resulted in a 5th order polynomial correlation model of the form:

$$\begin{aligned} &x = log_{10}(\text{Turbidity}), y = log_{10}(\mathrm{R_{rs}}(560)/\mathrm{R_{rs}}(665)) \\ &z = a_5 \cdot y^5 + a_4 \cdot y^4 + a_3 \cdot y^3 + a_2 \cdot y^2 + a_1 \cdot y + a_0 \\ &tu_{S2} = 10^z \end{aligned} \tag{2}$$

where tu_{S2} is the Sentinel-2 estimated turbidity in FNU, and

$$(a_0, a_1, a_2, a_3, a_4, a_5) = (1.547, -2.601, 8.021, -15.807, 142.329, -613.753), \tag{3}$$

where the fit is obtained by ordinary least squares. Figure 5(b) shows the correspondence obtained with the empirical band ratio fit to turbidity with an coefficient of determination of $R^2 = 0.687$. If we limit the to $R_{rs}(560)/R_{rs}(665) < 0.74$ then we see a significant decrease in the coefficient of determination to $R^2 = 0.362$, as we expected from our earlier observations.

Next, we performed a similar regression using the Gybe sensor reflectance from Fall 2021. Recall that we split the Gybe data set into a training set of 25 spectra and a test set of 18 spectra. The Gybe data (Figure 6(a)) shows a similar pattern as the S2 data (Figure 5(a)). One notable difference is that there are no extreme turbidity events (>200 FNU) during the Fall of 2021. A 3rd-order polynomial fit to the Gybe data yields,

$$\begin{aligned} &x = log_{10}(\text{Turbidity}), y = log_{10}(\mathrm{R_{rs}}(560)/\mathrm{R_{rs}}(665)) \\ &z = a_3 \cdot y^3 + a_2 \cdot y^2 + a_1 \cdot y + a_0 \\ &tu_{Gybe} = 10^z \end{aligned} \tag{4}$$

with coefficients

$$(a_0, a_1, a_2, a_3) = (1.744, -2.320, 2.938, 2.00) \tag{5}$$

where tu_{Gybe} is the Gybe estimated turbidity in FNU. The resulting coefficient of determination was $R^2 = 0.92$. The 5th order model is reported here only for sake of comparison since it performed marginally better with greater complexity. The 5th order model coefficients were $(a_0, a_1, a_2, a_3, a_4, a_5, a_6) = (1.788, -2.567, -7.611, 52.763, 332.956, -1467.613)$, with an $R^2 = 0.93$, MAE Training = 8.06, and MAE Test = 7.59. Part of the improved correlation can be attributed to the lack of year-to-year data in the Gybe spectral data set because of the limited time span of the data set, but part can also be attributed to the higher covariance between the Gybe sensor spectra and the turbidity data set. Limiting both data sets to only the 13 samples where the S2 images and Gybe are coincident, we estimated that the Pearson Correlation Coefficient of Gybe-Turbidity sensor pair was -0.87 whereas the S2-Turbidity sensor pair covariance was -0.77. We attribute the lower correlation of the the satellite-derived spectra to the the uncertainties introduced by the process of atmospheric correction. We applied Eq. (4) to the test set to gauge how well the correlation model handles out-of-sample data. Similar performance, as indicated by comparable values in the Mean Absolute Error (MAE) of training and test data sets, is shown in Figure 6(b).

2.2.2 Daily adjustments of Sentinel-2 spectra using a ground-based fiducial reference

The ground based data set contains more reflectance samples with a better correlations to water quality parameters than a satellite only data set. This suggests that when ground-based fiducial reference spectra are available, and particularly at the beginning of a calibration effort when there is limited satellite data, we chould consider a two-step modeling procedure. First, build a correlation model directly using ground-based spectra, and second, vicariously update the daily S2 Rrs values so that they are in line with the fiducial reference.

The overlapping pixels for a daily alignment of the Gybe sensor to the S2 spectra are indicated by the red circles in Figures 2(a) and 3(a). Figure 4 indicates typical scenarios for Chlorophyll-a and turbidity dominated situations. We next considered how to adjust the S2 spectra to bring it into alignment with the Gybe spectra, a process indicated schematically by arrow outlines in Figure 4. It is possible to construct many different maps that attempt, in some sense, to preserve the shape of the spectra [27]. Here we describe a method that restricts the map to a low order polynomial.

Ground-based and satellite derived spectra may be aligned by a polynomial function, which allows for offset (0th-order), gain (1st-order), and higher degree corrections. In the present study we limited the Sentinel 2 band set for alignment to B3, B4, and B5 since these are the only bands required by the selected water quality algorithms. We further simplified the correction procedure by applying the correction not to the bands directly, but to the band ratios B3/B4 and B5/B4 (since the reflectance band ratios are the independent variables for the water quality product algorithms and not the individual band reflectances). With these restrictions, a unique solution is available for the adjustment function. Appendix A provides more details for this method of spectral alignment.

The last step of the proposed method for a daily vicarious correction procedure is to apply the spectral alignment function derived from overlapping pixels to all the clear atmospheric pixels in the S2 image.

It is not obvious that the above class of algorithms for 'daily corrections' will, in the bulk, achieve the desired effect and it will need to be verified on a case-by-case basis, which we will accomplish here with data from downstream USGS gauging stations. However, if a significant source of uncertainty in the S2 retrievals are day-to-day variations that are uniform over the spatial range considered – say tens of kilometers of a river reach such as could be the case with aerosols or other atmospheric effects with long correlation lengths – then the vicarious adjustment described should improve S2 retrievals.

2.2.3 Validation of S2 turbidity products with daily fiducial reference based adjustments

To validate the S2-based water quality product maps we compared the values estimated at the De Soto site to distal locations with independent turbidity measurements, namely the USGS gauge on the Kansas River at Lake Quivira (16 miles downstream) and the USGS gauge at Randolph, MO on the Missouri River (38 river miles from De Soto).

We first checked the accuracy of the daily S2 daily adjustments using the Gybe sensor. This was accomplished by computing a 3x3 (9-pixel average) S2 estimate of turbidity at two locations, directly in the field of view of the Gybe sensor, and then at a point about 400 meters downstream, for all the days there were coincident S2 and Gybe spectra of good quality. Figure 7(a) shows the resulting time series, which (with one exception) shows good correspondence between the S2 estimates at separate sites that share almost identical water. The excellent consistency between the two locations is reflected in the near-perfect match exhibited in Figure 7(b). Figure 7(c) shows the match between the S2 estimate turbidity and the USGS gauge values – the coefficient of determination $R^2 = 0.87$ was used as a benchmark to gauge the accuracy of the S2 estimates at distal locations for which we have independent turbidity data.

Examining Figure 7(a) closely, we see one instance – 11 September 2021 – where there appears to be a substantial difference in turbidity values ($\sim$20 FNU) between the De Soto site and the test site 400 meters downstream. A closer look at the image for that day reveals a strip of haze directly above the test site, so that despite its proximity to the De Soto bridge image pixels, the satellite pixels at the test site have a higher reflectance due to a very localized atmospheric disturbance. The haze was so light that it was not noticed in the original RGB image but was more clearly revealed in an image constructed using the Red band (B4) alone, as shown in Figure 8.

Sixteen river miles downstream from De Soto is the USGS gauge near Lake Quivira on the Kansas River. Figure 9 shows the time series and turbidity match-ups between S2-derived turbidity values and the USGS gauge measurements. The coefficient of determination, $R^2 = 0.81$ (versus 0.72 for the unaligned spectra), indicates a moderate reduction in precision from the S2 turbidity derived values at De Soto. Further downstream, and on a different river system, at the Randolph USGS gauge on the Missouri river the precision is more substantially degraded as indicated by an $R^2 = 0.59$ (versus 0.61 for the unaligned spectra). This data is very limited, however our interpretation is that there is some evidence for the hypothesis that – within the same river system and watershed – it is possible to achieve S2-derived turbidity products using daily fiducial corrections over river reaches of tens of kilometers. Of course this hypothesis needs to be examined on a case-by-case basis in light of any knowledge about river inflows and outflows along a particular reach. Conversely, we would also expect to see significant degradation in the precision of fiducially corrected products when we different atmospheric conditions such as changes aerosol concentrations or constituents.

2.2.4 Sentinel-2 Chlorophyll concentration model

So-called 'red-edge' algorithms have proven useful for the detection of chlorophyll concentrations in turbid waters [20]. Therefore, we examined the correlation between the USGS chlorophyll time series and the Sentinel-2 band ratio formed from bands B4/B5 ($R_{rs}(665)/R_{rs}(705)$). Figure 11 shows that an estimate of chlorophyll can be made with a linear regression and results in a correlation model of the form:

$$chl_{S2} = 62.6 \cdot y - 58.2; \quad y = R_{rs}(665)/R_{rs}(705), \tag{6}$$

where the chlorophyll concentration is proportional to relative fluorescent units (RFU). Presumably, more refined multi-band algorithms [28] could improve on this result, but those were not explored in this study.

2.2.5 Sentinel-2 nitrate plus nitrite concentration models

Surrogate data modeling in water quality applications refers to using gauged water quality parameters, such as turbidity and chlorophyll concentrations, to estimate ungauged parameters, such as nutrient concentrations [29]. Surrogate models are site-specific and require calibration measurements with the target water quality parameters, and are typically estimated from regressions on multi-year time series [12]. Both linear [30] and nonlinear [17] surrogate data models have been developed and calibrated for the Lower Kansas River, and these could be used to provide estimates of nitrate plus nitrite concentrations from Sentinel-2 data. However, here we describe an alternative approach which, when applicable, provides substantially better correlation estimations ($R^2 > 0.9$) than those available from current surrogate data models (typically with an $R^2 < 0.8$).

A search of the time series provided by the USGS gauge at De Soto reveals several windows of time with high correlation between nitrate levels and other water quality parameters. These windows of correlations have been previously labeled and analyzed in the context of concentration-discharge (C-Q) 'hysteresis curves' [31]. Many studies connect the qualitative shape of these hydrologic hysteresis curves to specific land-water runoff processes, such as how nutrient concentrations in soils do (or do not) limit the concentrations observed in runoff discharge [32].

For instance, a high correlation between nitrate concentrations and turbidity in the Kansas river is observed in an image from 10 February 2023. Figure 12(a) shows a large inflow of sediment-laden waters from sources such as Stranger Creek and the Wakarusa River further upstream. We hypothesize that the nitrate loads are not source-limited during this period, so there is a direct correlation between turbidity, sediment concentrations, and nitrates from stormwater runoff, as Figure 12(b) appears to indicate. The water that passes under the bridge at De Soto 9:00 CST 10 February 2023 is advected downstream arriving at the USGS gauge on the Kansas River near Lake Quivira at 3:00 CST on 11 February 2023, as determined by correlating the turbidity curves at each site. The transit time is 18 hours over a distance of 16 river miles, or an approximate mean river speed of 0.9 mph. Thus, the values in our correlation curve are also valid for 14.4 miles (0.9 mph $\cdot$ 16 hr), or $\sim$ 23 km of river reach east of De Soto, KS — assuming, of course, that there are no other major influxes of turbid laden water in the reach, or if there are, then they share a similar sediment-nitrate make up. This assumption was checked by a qualitative inspection of the remote sensing imagery and appears valid for this limited time window.

These high turbidity events are especially important to gauge accurately because they carry the bulk of the yearly nitrate loading [33]. Thus, gauging them with higher accuracy surrogate models, even if they are only of intermittent utility, should improve both event and yearly nitrate loading estimations.

3 Results

This section looks at a few examples of the generation of water quality product maps and 'virtual' gauging for the Kansas River. These remote sensing data products not only help with understanding biogeochemical processes within the Kansas River but can also inform issues around water sampling and gauging.

3.1 Transverse mixing at the confluence of Missouri and Kansas Rivers

Figure 13(a) shows the confluence of the Kansas and Missouri rivers on 11 September 2021. The Kansas River entering the Missouri River from the west has a high sediment load ($\sim$130 FNU), which appears to be initially confined to the southern bank of the Missouri River. This type of confinement can occur when a slower-moving river converges with a faster-moving river, and the mixing interface has been described theoretically using a Kelvin-Helmholtz instability [34]. Recent studies have also shown how to estimate measures of the transverse mixing that occurs at confluent river flows, as shown in this example [35]. Moving seven miles upstream on the Missouri River to the USGS gauging station at Randolph, Figure 13(b) reveals that there is still a significant gradient of sediment concentration between the North Bank, where the USGS gauging station is located, and the South Bank of the Missouri River.

A look into the historical record of Sentinel-2 images shows that such mixing patterns between the Missouri and Kansas rivers are not uncommon; that is, a distinct mixing interface exists in the intermediate mixing regime for several miles. The USGS sensors at Randolph, MO, have changed locations over the years, so an understanding of typical transverse sediment distributions can inform the interpretation of the historical time series as well as provide guidance for future sensor placements.

3.2 Longitudinal virtual gauging of a turbidity slug in the Kansas River

The following example looks at monitoring turbidity slugs generated from storm runoff. These turbidity slugs often carry high nutrient loads and are particularly easy to detect in the Kansas River with remote sensing. Figure 14(a), a Sentinel-2 image from 28 February 2023, shows the leading edge of a long turbidity slug approaching the city of Lawrence. The slug was generated from a storm near Topeka about 30 miles upstream. During the late evening of 27 February 2023, over an inch of rain fell in the Topeka region, resulting in substantial storm runoff with high sediment loads. The imagery (Figs. 13(b,c)) shows a clear gradient from brown water to greener baseflow water between Lawrence and the town of Eudora, located ten river miles downstream.

The longitudinal structure of the leading edge of the turbidity slug can be measured by the using remote sensing 'virtual gauges.' A sequence of pixels is selected so that they are located approximately in the middle of the Kansas River, and also avoid gravel bars. The pixels are spaced approximately 0.5 miles apart. Water quality product values are extracted at each pixel and plotted as illustrated in Figure 14(d). This particular plot uncovers an inverse relation between turbidity and chlorophyll concentration as the virtual gauging location moves downstream. Finer details are also evident in the plot, such as the longitudinal sediment concentration showing a rapid fall off before the bridge (Fig. 14(b)) on the westmost section of the Kansas River (river miles 54-52), and then a more gradual decline further downstream (river miles 52-38) as shown in Figure 14(d)).

Searching for the origins of the slug, we observed the first significant inflow of sediment-laden stormwater in the 28 February 2023 image is located at the confluence of Mill Creek (17 miles west of Topeka) and the Kansas River (Fig. 15(a)). The turbidity slug is long, roughly 50 river miles from tail to head (Mill Creek to Lawrence). A well-defined mixing interface is visible, producing a impressionistic-like image as the merging waters weave around the gravel bars. A detailed look at the turbidity gradient across the mixing interfaces can be probed by virtual gauging. Figure 15(b) shows a plot for an imaginary boat track crossing in and out of the mixing interfaces. The sharp transitions at the mixing interface are easily detected as the path of the virtual gauging crosses from the green base flow of the Kansas River to braids of brown water emerging from Mill Creek to the south and Cross Creek in the north. In the visible imagery, the braids appear to last downstream as far as just west of Topeka – so in this instance, a river reach of $\sim$15 miles is required before the flow is well mixed in the transverse direction [36].

3.3 Nutrient concentration map of the Kansas River near the Lawrence, KS

Figure 16(a) shows the time series between nitrate plus nitride concentration and turbidity for the USGS gauge at De Soto for the turbid slug exists in the image from 28 February 2023. The correspondence is good enough to estimate the nutrient concentration from turbidity with high confidence ($R^2 = 0.946$ in Fig. 16(b)). As a point of comparison a nonlinear model trained on a complete historical time series between 2016-2023, not temporally filtered, produced an $R^2 = 0.72$[17]. The parcels of water at Lawrence during the S2 overpass at 11:22 CST reach the De Soto sensor about 13 hours later since the mean surface velocity is approximately 1.6 mph, which was determined by cross-correlating the S2 turbidity transect in Lawrence with the turbidity signal at De Soto. There are two potentially significant inflows between Lawrence and De Soto: the Wakarusa River (see Fig. 14(c)) and Stranger Creek, and neither shows a large influx of sediment loads in the S2 image. Therefore, we used the following linear correlation model to estimate nitrate plus nitrite concentration from turbidity:

$$ni_{S2} = 0.00467 \cdot tu_{S2} + 0.165. \tag{7}$$

which is only applicable to the subsection of the 28 February 2023 S2 image that sits within the advection time window.

Figure 17 shows the nitrate concentration estimate based on Eq. (7). A linear scale for the nitrate plus nitrite concentration product map is shown in red. The remaining area shows the (pseudo) S2 RGB image. Of course, this image was chosen because it nicely illustrates the start of an extended period ($\sim$ 30 hours = 50 hours / 1.6 mph) of degraded (high sediment load and nutrient load) water quality from the Kansas River in the Lawrence.

4 Discussion

Remote sensing imagery opens the door to a wealth of new insights into the processes affecting the waters of the Kansas River, as well as informing issues concerned with water quality gauging and sampling. The Sentinel-2 derived water product maps augment the USGS high frequency *in situ* gauging by revealing patterns in both the downstream and cross-channel structures of the biogeochemical process in the Kansas River. The bulk of this paper discussed the methods used to develop spatially dense water quality product maps. The examples illustrate the resolution that is possible with current operational satellites. Though we did not provide details on the implications of the map data for ecological services, we do illustrate that the spatial resolution is sufficient to follow inflows from creeks (Stranger and Mill) and rivers (Wakarusa) upstream to further interrogate land/water processes. Some applications where water quality maps could be used include the identification of upstream locations of (or suggestions for) vegetative filter strips, or evaluating the efficacy of restoration efforts by providing virtual gaging of sediment transport and water clarity around inflows and outflows of wetlands. Similar monitoring could inform activities such as watering and grazing operations or the location of feeding systems.

As shown in the examples, much of the sediment load in the Lower Kansas River is due to creeks (e.g., Stranger) that are not regulated by large control structures such as the Clinton Reservoir. Again, virtual gauging of these undergauged inflows should enable a better understanding of the source and fate of sediment transport and its associated biogeochemical properties within the Lower Kansas River. For instance, some preliminary work shows that it is possible to identify inflows not just from overland processes but also from tiled fields, which can provide very rapid transport of nutrients into the Kansas River after storm events.

This study demonstrates ways in which the fusion of remote sensing imagery and daily high-frequency data, both in water gauging, and above-water radiometric sensors, enables more accurate water quality maps.

Because of the short time frame for data collection with the ground based radiometer, the study only provides limited evidence that modest improvements in surface spectral reflectance estimations from satellite imagery are possible by using daily alignments with a single point fiducial ground-based reference. That said, the method for spectral corrections utilized here is very simple, and it is quite likely that more sophisticated techniques, such as those using Bayesian inference methods [37], could result in more significant reductions in the covariance between satellite, ground based reflectance values, and water quality target parameters.

Perhaps of more immediate value is the observation that maps of water quality can be improved by exploiting the temporal windows of high correlation between various water quality parameters which are often observed during storm runoff events or reservoir releases. These correlations have been studied in the context of hydrologic concentration-discharge hysteresis analysis [38], but their utlitiy for water quality surrogate data modeling has, to the best of our knowledge, not been utilized before in the construction of remote sensing based water quality maps. The observation that the water parcels used in the daily calibration of the remote sensing water quality maps are the same water parcels measured by the fixed location gauging (using Lagrangian transport to interchange space and time measurements) opens a door to building better maps of water quality. The periods of high correlation, while intermittent, are also easy to identify in the high-frequency *in situ* data streams and often occur during events that transport significant quantities of organic and inorganic materials. Thus, the use of temporally windowed data, in remote sensing surrogate models of water quality, should lead to better estimates of both event and seasonal biogeochemical loadings and enable a sharper view of their spatial patterns.

Acknowledgments

We thank Dr. Thomas Williams and his team at the USGS Kansas Water Science Center for installing and maintaining the instruments at the De Soto, KS, Super Gage site, including setting up the spectral radiometer. This work was supported in part by DOE Grant DE-SC0020843.

Appendix: Daily updates of water quality band ratios using a fiducial spectral reference

Denote the Sentinel-2 spectral bands as $q_3 = R_{rs}^{sentinel}(560)$, $q_4 = R_{rs}^{sentinel}(665)$, and $q_5 = R_{rs}^{sentinel}(705)$. Similarly, let the Gybe spectral bands be: $p_3 = R_{rs}^{gybe}(560)$, $p_4 = R_{rs}^{gybe}(665)$, and $p_5 = R_{rs}^{gybe}(705)$. Then the Sentinel-2 turbidity product band ratios is $s_T = q_3/q_4$ and the chlorophyll product band ratio is $s_C = q_5/q_4$. Similarly, the Gybe sensor band ratios are $r_T = p_3/p_4$ and $r_C = p_5/p_4$. Consider the maps from

$$\mathrm{MAP} : (s_T, s_C) \longrightarrow (r_T, r_C).$$

A linear map has the form:

$$\mathrm{G} : (\tilde{s}_T, \tilde{s}_C) = (g_T \cdot s_T, g_C \cdot s_C) \tag{8}$$

with $g_T = r_T/s_T$, $g_C = r_C/s_C$, which we also call the 'gain' map. The two gain constants calculated at the overlapping reference pixels are applied to every pixel in the scene, thereby 'pulling' them into a daily alignment with the Gybe reference spectrum. The *tilde* indicates a value after a daily correction is applied. The next simplest class of maps are 'affine maps' consisting of an offset and a gain, which is determined by solving the set of linear equations:

$$m \cdot (s_T, s_C) + b = (r_T, r_C).$$

Solving for m and b we find:

$$m = \frac{(r_T - r_C)}{(s_T - s_C)}; \quad b = r_T - \frac{(r_T - r_C)}{(s_T - s_C)} \cdot s_T$$

If we denote the corrected Sentinel-2 spectra by $\tilde{\mathbf{s}} = (\tilde{s}_T, \tilde{s}_C)$, then the affine map

$$\mathrm{A} : \tilde{\mathbf{s}} = m \cdot \mathbf{s} + b$$

with $\mathbf{s} = (s_T, s_C)$ and at the reference pixels is exactly equal to $\mathbf{r} = (r_T, r_C)$ by construction. More generally, if the number of band ratios to be adjusted ($\mathbf{s} = (s_1, s_2, s_3, ..., s_n)$) is not equal to the number of fitting parameters, then a singular value decomposition [27] can be computed to find the best fit in the mean of the input and reference spectra. Also note that the same affine transformation applies to the original Sentinel R_{rs} bands ($\mathbf{q}_l = (q_T, q_C)$). The adjustments are well-defined as long as $(s_T - s_C)$ or $(r_T - r_C)$ does not equal zero. If the differences are close to zero, the adjustment constants could be very large, leading to problematic corrections.

References

[1] Megan Rush et al. Lower Kansas River watershed restoration and protection strategies (WRAPS) Plan 2021. Technical report, Kansas Alliance for Wetlands and Streams, 2021.

[2] Debra Baker, Donald Huggins, Steve Cringan, Robert Angelo, and Heidi Mehl. Environmental flow requirements for the Kansas River: Background literature review and summary. Technical report, U.S. Army Corps of Engineers, Kansas City District, May 2022.

[3] Kansas lower republic basin total maximum daily load. `https://www.kdhe.ks.gov/DocumentCenter/View/14018/Crooked-Creek-TP-PDF`. Accessed: 2024-02-20.

[4] `https://kansasriver.org/`. Accessed: 2024-02-20.

[5] `https://www.nature.org/en-us/get-involved/how-to-help/places-we-protect/kansas-kaw-river/`. Accessed: 2024-02-20.

[6] `https://www.usgs.gov/centers/kansas-water-science-center/science/water-quality-monitoring-lower-kansas-river-basin`. Accessed: 2024-02-20.

[7] Nima Pahlevan, S Sarkar, BA Franz, Sundarabalan V Balasubramanian, and Jiaying He. Sentinel-2 multispectral instrument (MSI) data processing for aquatic science applications: Demonstrations and validations. *Remote sensing of environment*, 201:47–56, 2017.

[8] Miles S Finch, David J Hydes, Charles H Clayson, Bernhard Weigl, John Dakin, and Pat Gwilliam. A low power ultra violet spectrophotometer for measurement of nitrate in seawater: introduction, calibration and initial sea trials. *Analytica Chimica Acta*, 377(2-3):167–177, 1998.

[9] Saman Razavi, Bryan A Tolson, and Donald H Burn. Review of surrogate modeling in water resources. *Water Resources Research*, 48(7), 2012.

[10] Mohammad Haji Gholizadeh, Assefa M Melesse, and Lakshmi Reddi. A comprehensive review on water quality parameters estimation using remote sensing techniques. *Sensors*, 16(8):1298, 2016.

[11] `http://www.gybe.eco`. Accessed: 2024-02-20.

[12] Nicholas Tufillaro, Bryan Piazza, Sheila Reddy, Joseph Baustian, Dan Sousa, Philipp Grötsch, Ivan Lalović, Sara De Moitié, and Omar Zurita. Linking optical data and nitrates in the lower Mississippi River to enable satellite-based monitoring of nutrient reduction goals. *Ecohydrology*, 02 2024.

[13] Quinten Vanhellemont and Kevin Ruddick. Atmospheric correction of metre-scale optical satellite data for inland and coastal water applications. *Remote sensing of environment*, 216:586–597, 2018.

[14] Kevin Ruddick et al. A review of protocols for fiducial reference measurements of water-leaving radiance for validation of satellite remote-sensing data over water. *Remote Sensing*, 11(19):2198, 2019.

[15] Peter Gege and Philipp Grötsch. A spectral model for correcting sunglint and skyglint. *Proceedings of Ocean Optics XXIII 2016*, pages 1–10, 2016.

[16] Philipp Grötsch, Robert Foster, and Alexander Gilerson. Exploring the limits for sky and sun glint correction of hyperspectral above-surface reflectance observations. *Applied Optics*, 59(9):2942–2954, 2020.

[17] Nicholas Tufillaro. A manifold learning perspective on surrogate modeling of nitrates in the Kansas River. *IWA Water Practice and Technology*, 19(7), 2024.

[18] Brian Timmer, Luba Y Reshitnyk, Margot Hessing-Lewis, Francis Juanes, and Maycira Costa. Comparing the use of red-edge and near-infrared wavelength ranges for detecting submerged kelp canopy. *Remote Sensing*, 14(9):2241, 2022.

[19] Ana Inés Dogliotti, KG Ruddick, B Nechad, David Doxaran, and Els Knaeps. A single algorithm to retrieve turbidity from remotely-sensed data in all coastal and estuarine waters. *Remote sensing of environment*, 156:157–168, 2015.

[20] Sachidananda Mishra and Deepak R Mishra. Normalized difference chlorophyll index: A novel model for remote estimation of chlorophyll-a concentration in turbid productive waters. *Remote Sensing of Environment*, 117:394–406, 2012.

[21] Chuanmin Hu, Zhongping Lee, and Bryan Franz. Chlorophyll algorithms for oligotrophic oceans: A novel approach based on three-band reflectance difference. *Journal of Geophysical Research: Oceans*, 117(C1), 2012.

[22] Andrew P Rutter, David C Snyder, Elizabeth A Stone, Brandon Shelton, Jeff DeMinter, and James J Schauer. Preliminary assessment of the anthropogenic and biogenic contributions to secondary organic aerosols at two industrial cities in the upper midwest. *Atmospheric Environment*, 84:307–313, 2014.

[23] Philipp Grötsch, Peter Gege, Stefan GH Simis, Marieke A Eleveld, and Steef WM Peters. Variability of adjacency effects in sky reflectance measurements. *Optics Letters*, 42(17):3359–3362, 2017.

[24] Rejane S Paulino, Vitor S Martins, Evlyn MLM Novo, Claudio CF Barbosa, Lino AS de Carvalho, and Felipe N Begliomini. Assessment of adjacency correction over inland waters using sentinel-2 msi images. *Remote Sensing*, 14(8):1829, 2022.

[25] Bouchura Nechad, Kevin G Ruddick, and YJRSoE Park. Calibration and validation of a generic multisensor algorithm for mapping of total suspended matter in turbid waters. *Remote Sensing of Environment*, 114:854–866, 2010.

[26] Kevin G Ruddick, Vera De Cauwer, Young-Je Park, and Gerald Moore. Seaborne measurements of near infrared water-leaving reflectance: The similarity spectrum for turbid waters. *Limnology and Oceanography*, 51(2):1167–1179, 2006.

[27] John C Gower and Garmt B Dijksterhuis. *Procrustes problem*, volume 30. OUP Oxford, 2004.

[28] Alexander Gilerson, Michael Ondrusek, Maria Tzortziou, Robert Foster, Ahmed El-Habashi, Surya Prakash Tiwari, and Sam Ahmed. Multi-band algorithms for the estimation of chlorophyll concentration in the chesapeake bay. In *Remote Sensing of the Ocean, Sea Ice, Coastal Waters, and Large Water Regions 2015*, volume 9638, pages 60–71. SPIE, 2015.

[29] T.J. Rasmussen, A.C. Ziegler, and P.P. Rasmussen. Estimation of constituent concentrations, densities, loads, and yields in lower Kansas River, northeast Kansas, using regression models and continuous water-quality monitoring, January 2000 through December 2003. Technical report, USGS, 2005.

[30] Thomas J Williams. Linear regression model documentation and updates for computing water-quality constituent concentrations or densities using continuous real-time water-quality data for the Kansas river, Kansas, July 2012 through September 2019. Technical report, US Geological Survey, 2021.

[31] Oladipo Bolade and Amy T Hansen. Inferring drivers of nitrate and sediment event dynamics from hysteresis metrics for two large agricultural watersheds. *Hydrological Processes*, 37(9):e14969, 2023.

[32] Shannon L Speir, Lucy A Rose, Joanna R Blaszczak, Dustin W Kincaid, Hannah M Fazekas, Alex J Webster, Michelle A Wolford, Arial J Shogren, and Adam S Wymore. Catchment concentration–discharge relationships across temporal scales: A review. *Wiley Interdisciplinary Reviews: Water*, 11(2):e1702, 2024.

[33] Taryn Waite, Kathi Jo Jankowski, Denisw A Bruesewitz, Molly Van Appledorn, Megan Johnston, Jeffrey N Houser, Douglas A Baumann, and Barbara Bennie. River geomorphology affects biogeochemical responses to hydrologic events in a large river ecosystem. *Water Resources Research*, 59(7):e2022WR033662, 2023.

[34] *On Shallow Mixing Interfaces and Their Relevance for Understanding Mixing at River Confluences*, volume Direct and Large Eddy Simulation XII. Springer, 2020.

[35] M Umar, Bruce L Rhoads, and Jonathan A Greenberg. Use of multispectral satellite remote sensing to assess mixing of suspended sediment downstream of large river confluences. *Journal of Hydrology*, 556:325–338, 2018.

[36] AN Sukhodolov, OO Shumilova, GS Constantinescu, QW Lewis, and BL Rhoads. Mixing dynamics at river confluences governed by intermodal behaviour. *Nature Geoscience*, 16(1):89–93, 2023.

[37] Mortimer Werther, Daniel Odermatt, Stefan GH Simis, Daniela Gurlin, Moritz K Lehmann, Tiit Kutser, Remika Gupana, Adam Varley, Peter D Hunter, Andrew N Tyler, et al. A bayesian approach for remote sensing of chlorophyll-a and associated retrieval uncertainty in oligotrophic and mesotrophic lakes. *Remote Sensing of Environment*, 283:113295, 2022.

[38] Andreas Musolff, Qing Zhan, Remí Dupas, Camille Minaudo, Jan H Fleckenstein, Michael Rode, Joni Dehaspe, and Karsten Rinke. Spatial and temporal variability in concentration-discharge relationships at the event scale. *Water Resources Research*, 57(10):e2020WR029442, 2021.

Table 1: USGS Stations

Name	USGS Number	Location	River Mile	Sensor Data of Interest	Comments
De Soto	06892350	(38.983, -94.965)	Kaw 31	Turbidity, Chlorophyll, Nitrate plus Nitrite	20 River Miles downstream of Bowerstock Dam in Lawrence
Lake Quivira	06892518	(39.046, -94.789)	Kaw 15	Turbidity, Chlorophyll	WaterOne Dam, 16 River Miles downstream of De Soto
Randolph	06893060	(39.152, -94.494)	Missouri 360	Turbidity	Gage Station on the North bank East of Hwy 435 Bridge

Table 2: Other Sites of Interest

Name	Location	River Mile	Comment
Junction City	(39.060, -96.800)	169.5	
Mill Creek	(39.109, -95.993)	104.1	
Topeka Wier USGS 06888990	(39.072, -95.716)	87	Water Treatment Plant, Turbidity, Chlorophyll
Topeka	(39.067, -95.651)	82.9	New Sardou Bridge
Lawrence Water Treatment Plant	(38.981, -95.239)	52.3	52 River Miles downstream from Mill Creek
Bowerstock Dam	(38.975, -95.235)	51.8	
Eudora	(38.956, -95.097)	42.4	10 River Miles downstream from Lawrence
Mouth of Kaw	(39.115, -94.610)	0	Confluence with Missouri River

Figure 1: The Gybe hyperspectral radiometer installed above the Kansas River at De Soto, KS colocated with USGS super gage site measuring nitrate plus nitrite.

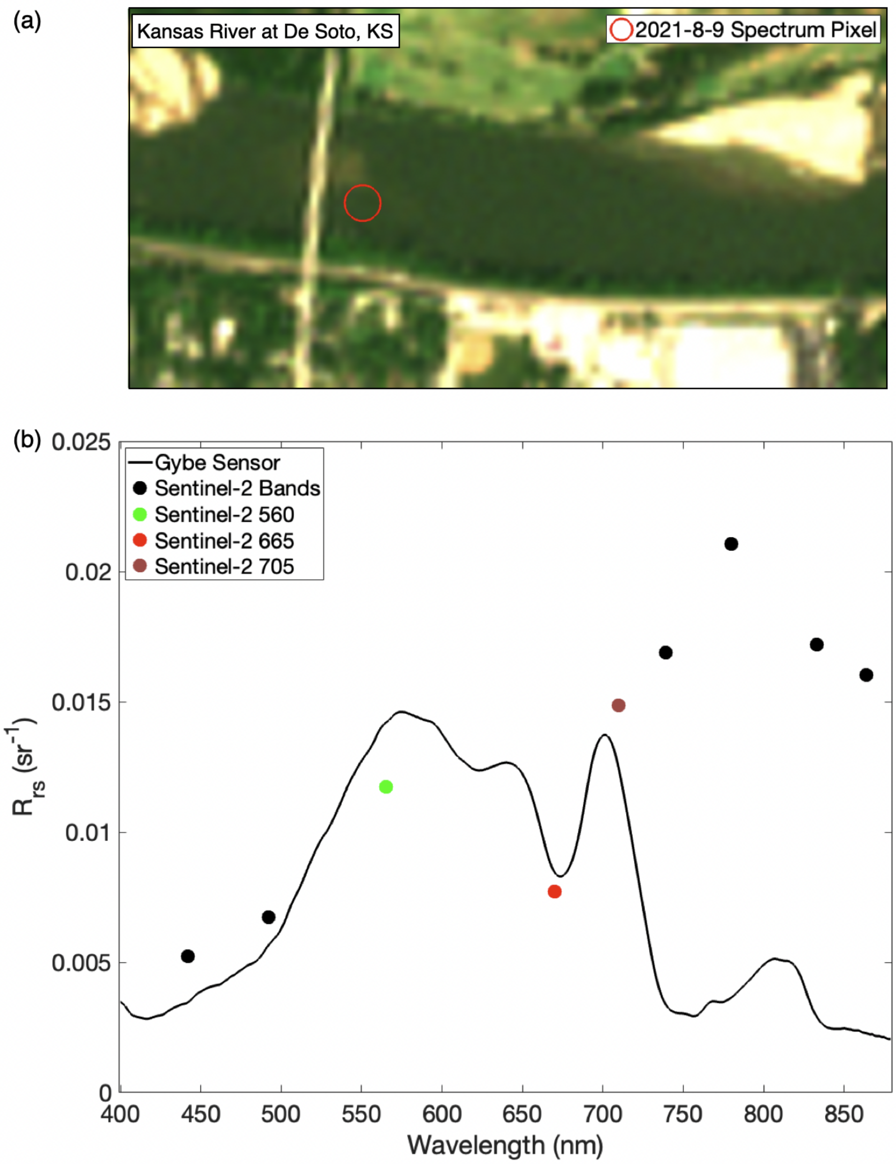

Figure 2: (a) Sentinel-2 image of Kansas River at De Soto, KS, on 9 August 2021 at 12:12 CDT (17:12 GMT). (b) Remote sensing reflectance spectra collected from the middle of the bridge looking approximately Northeast. The green water has a chlorophyll fluorescence (fChl) of 7.2 relative fluorescence units (RFU). The elevated Sentinel-2 reflectance values in the Red-IR (> 730 nm) are due to atmospheric correction artifacts from 'adjacency effects' as described in [24]. The Sentinel-2 bands are referenced by nominal wavelengths.

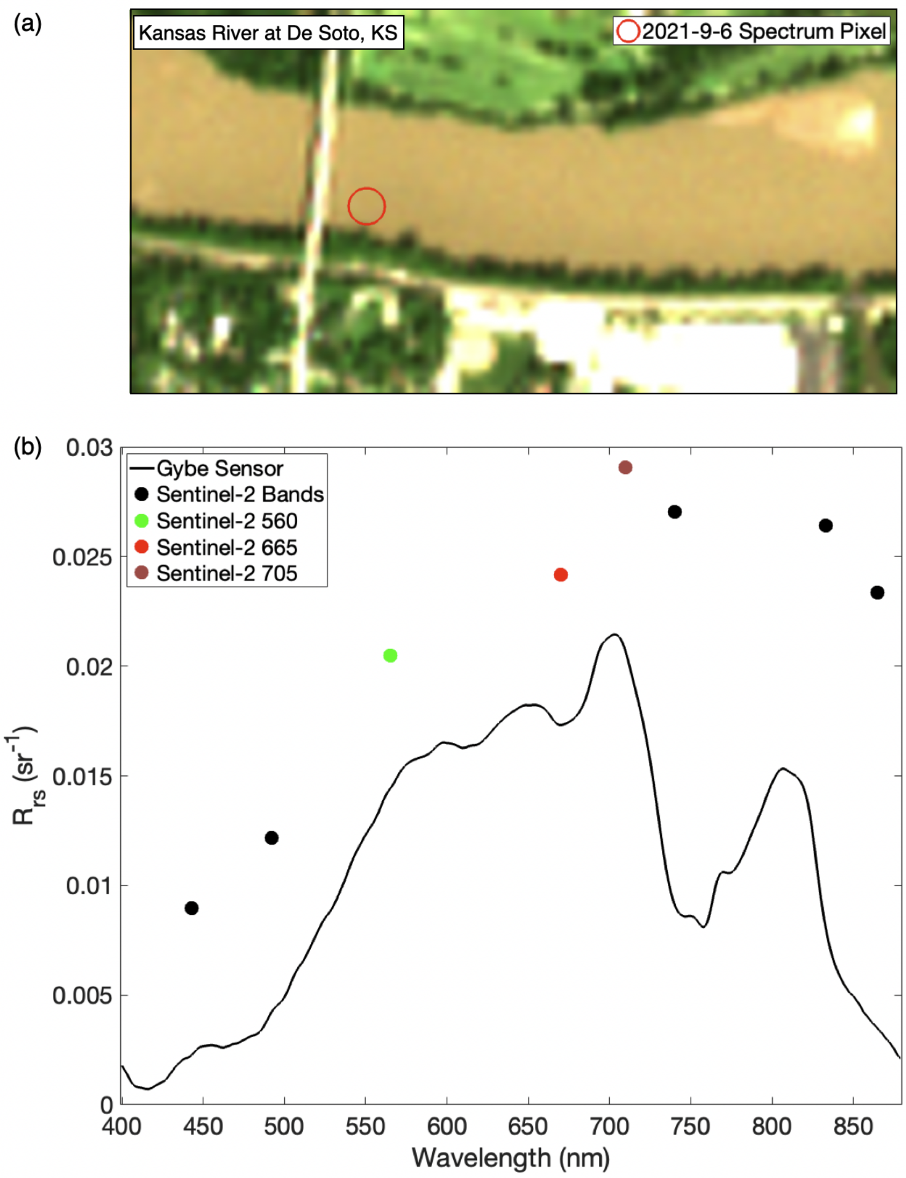

Figure 3: (a) Sentinel-2 image of Kansas River at De Soto, KS, on 6 September 2021 at 12:22 CDT (17:22 GMT). (b) Remote sensing reflectance spectra were collected from the middle of the bridge looking approximately Northeast. The brown water has a high turbidity (118 FNU), which causes a strong backscatter that is evident in the elevated Rrs values especially between 600-700 nm.

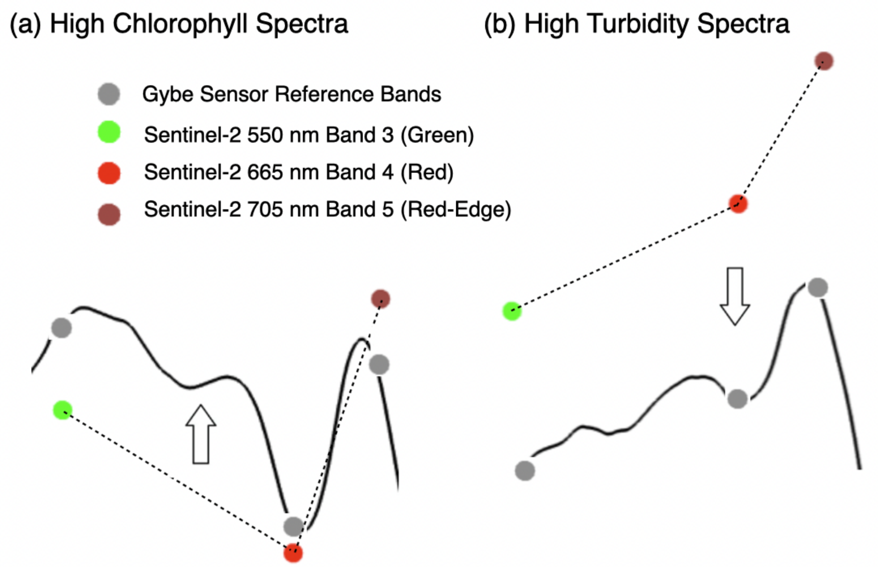

Figure 4: (a) Sentinel-2 and Gybe spectra as typically observed for low turbidity water (b) Sentinel-2 and Gybe spectra as typically observed for high turbidity water. The systematic increase in slope between bands 3 and 4, as turbidity increases, is due to the reduction in the wavelength-dependent effects of water absorption due to an increase in backscatter. The arrows indicate a map that provides an empirical daily vicarious correction to the Acolite derived S2 spectrum to bring it into better correspondence with the Gybe field spectra.

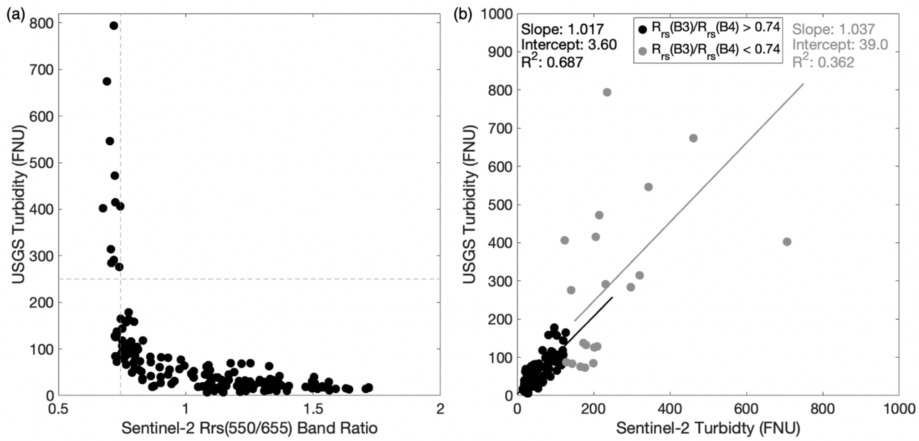

Figure 5: (a) Correspondence between USGS turbidity values and Sentinel-2 band ratio values formed from $R_{rs}(560)/R_{rs}(665)$. A good correlation is observed for values of turbidity below ∼200 FNU. This suggests limiting the correlation model to band ratios above ∼0.74, as indicated by the dotted lines separating the regions containing normal and extreme turbidity events (b) For normal turbidity events, a good correlation model can be established as indicated by the R^2 value of 0.687. For extreme events ($R_{rs}(560)/R_{rs}(665) > 0.74$) an estimate of turbidity has a much greater level of uncertainty.

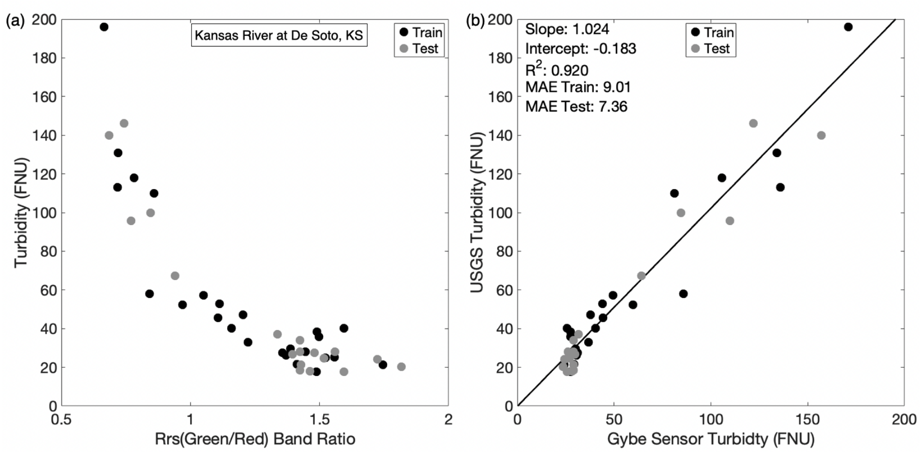

Figure 6: Gybe sensor turbidity product calibration. (a) Match up between USGS Turbidity and Gybe spectral radiometer band ratio, $R_{rs}(560)/R_{rs}(665)$ (b) Fit of USGS turbidity with turbidity predicted from the Gybe sensor after calibration to a third-order polynomial model. There are 25 points in the training set and 18 in the test set, which consists of spectra and turbidity values measured at the De Soto, KS site during the Fall 2021. The comparable values of the maximum absolute error (MAE) of the training and test sets indicate good out-of-sample performance of the estimated turbidity product.

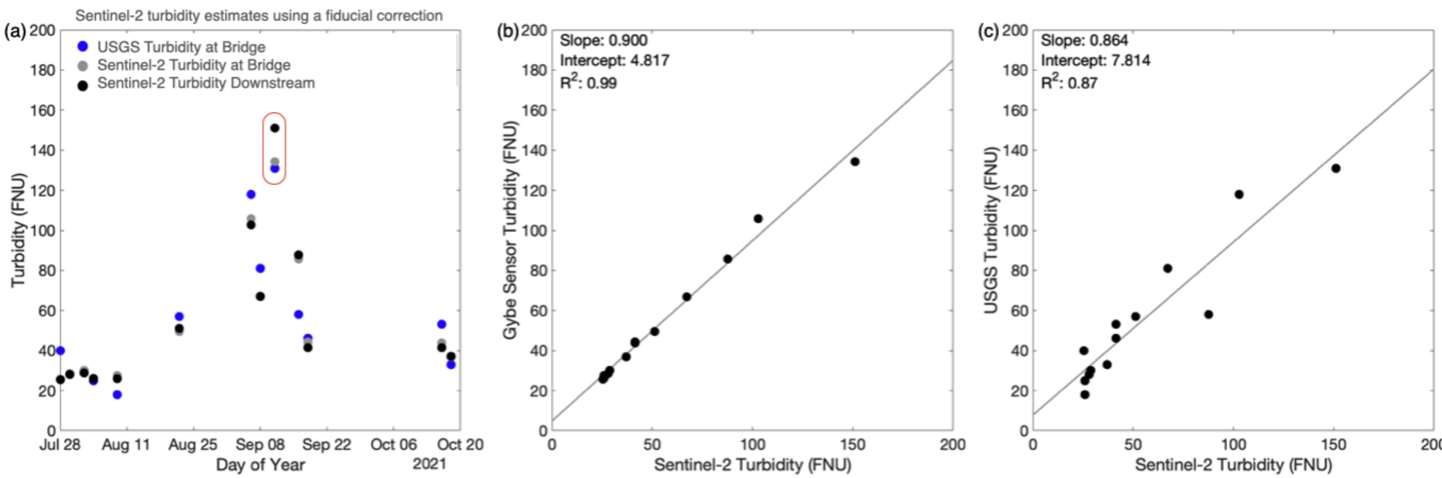

Figure 7: Test of the daily vicarious adjustment of the Sentinel-2 turbidity product by comparing the turbidities at the De Soto bridge with those estimated by Sentinel-2 (with the vicarious adjustment) in close proximity, ($\sim$400m) downstream. The test assumes that both the water color and sky conditions are identical at the two locations – in which case, the S2 estimates of turbidity should be identical. (a) Time series comparing the Sentinel-2 turbidities (with fiducial corrections) at the De Soto Bridge (gray dots) with turbidites at a downstream location (black dots). A comparison to the USGS turbidity values (blue dots) is also shown. A large discrepancy between the black and gray points indicates that the application of the vicarious daily adjustment may not be valid. The red oval highlights that the image from 11 September 2021 appears to fail the validation test. (b) The one-to-one plot of the black and gray dots in Fig. 7(a). The $R^2 = 0.99$ is a gauge of the accuracy of the S2 alignment to the Gybe turbidity product (under the assumed clear sky conditions). (c) The one-to-one plot of the gray and blue dots in Fig. 7(a). Match up between the Gybe turbidity product and the USGS values at the De Soto bridge. The $R^2 = 0.87$ is a gauge of the accuracy the Gybe turbidity product relative to the USGS turbidity product.

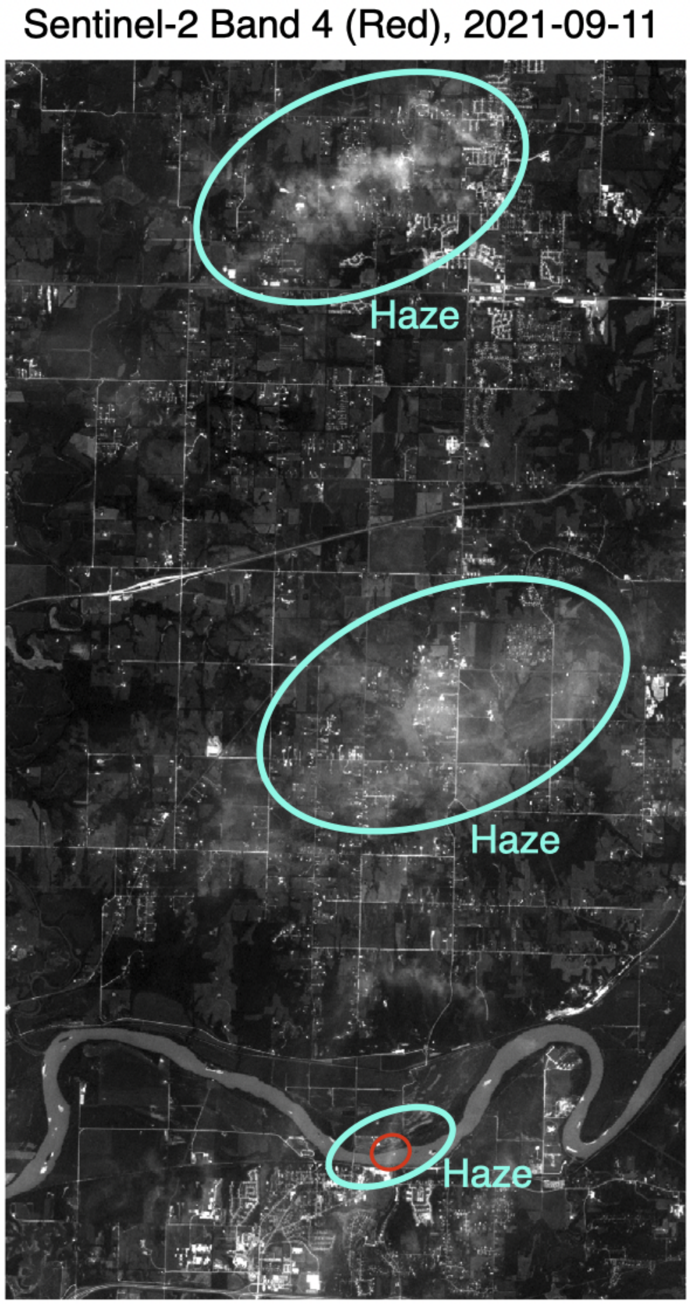

Figure 8: Sentinel-2 image of the De Soto, KS region from 2021-09-11 showing haze (highlighted by cyan ovals). A small patch of haze (red circle) is just above the test water patch and is the origin of the discrepancy indicated by the red oval in Fig 7(a).

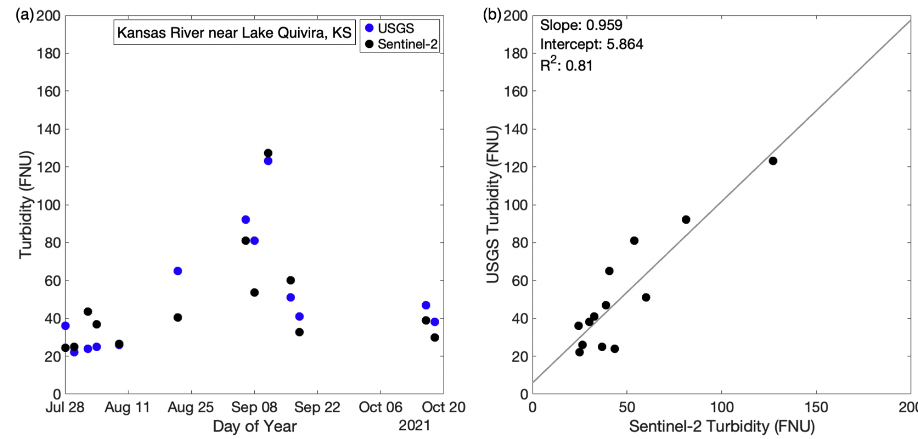

Figure 9: (a) Time series comparing Sentinel-2 turbidity estimates to USGS values on the Kansas River near Lake Quivira during the Fall of 2021. (b) An $R^2 = 0.81$ indicates that, at least for this particular 16-mile river reach, the fiducial corrections to the S2 turbidity values are better than the unadjusted S2 estimates.

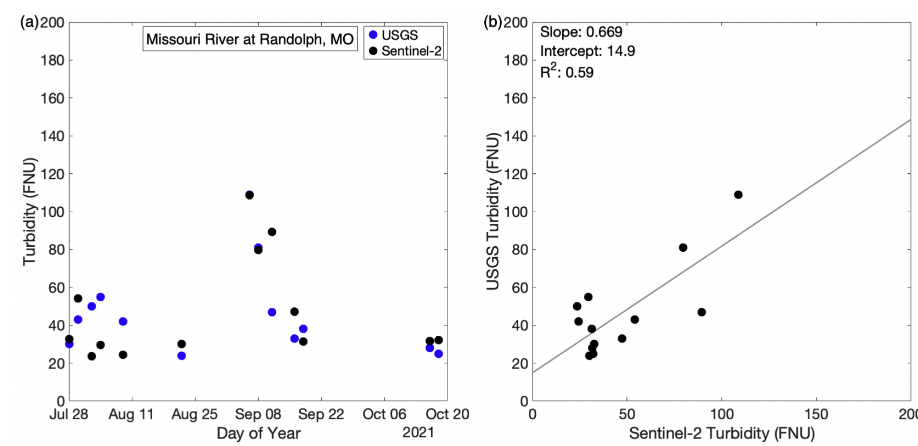

Figure 10: (a) Time series comparing Sentinel-2 turbidity estimates to USGS values on the Missouri river near Randolph during the Fall 2021. This patch of water is 38 river miles downstream from De Soto and on a different river and watershed. (b) An $R^2 = 0.59$ indicates that the fiducial corrections to the S2 turbidity values are no better than the unadjusted S2 estimates (see Fig 5(b))

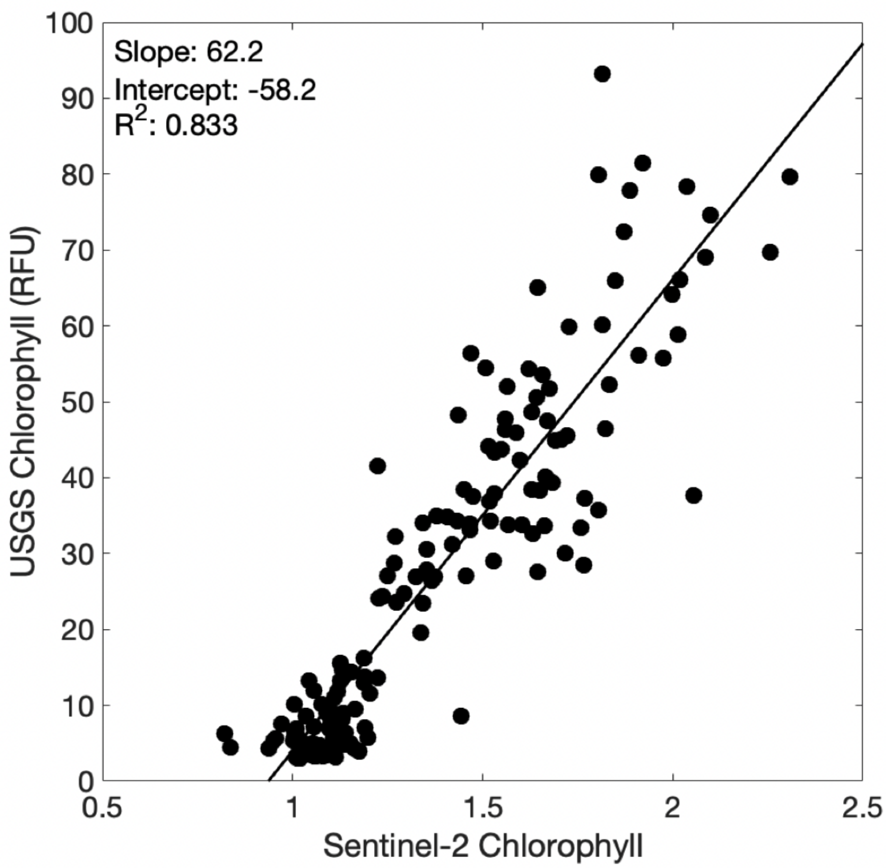

Figure 11: Linear regression showing a correlation between USGS Chlorophyll time series (fChl in Relative Fluorescent Units) and a Sentinel-2 band ratio formed from bands B5/B4 ($R_{rs}(705)/R_{rs}(665)$).

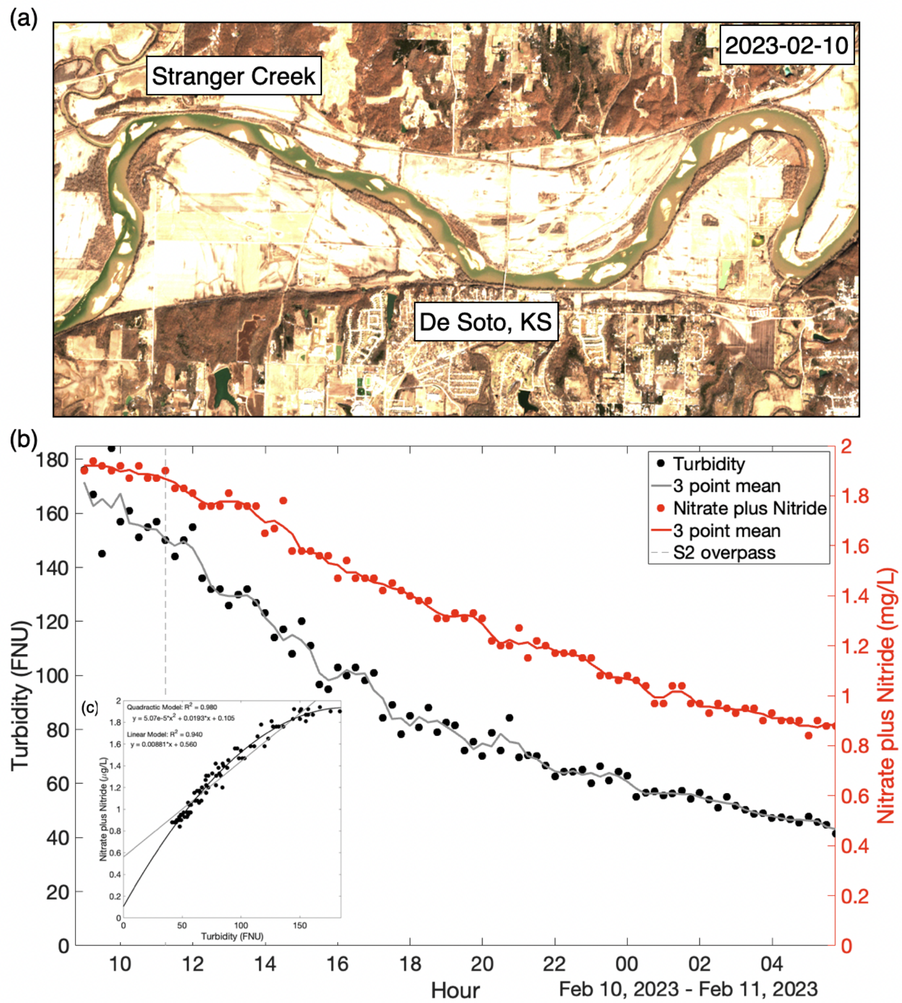

Figure 12: Example of a Sentinel-2 image around De Soto, KS, on 10 February 2023 showing that accurate daily estimation of nutrient target products are possible during periods of high correlations between the target product and remote sensing products such as turbidity: (a) (pseudo) RGB image of Kansas river showing high inflow of turbidity from sources such as Stranger Creek, (b) Time series of turbidity and nitrate plus nitrite concentrations from USGS gauge at De Soto, KS, (c) Empirical correlations show excellent correspondence between turbidity and nitrate plus nitrite concentration during a 16-hour window beginning at 9:00 CST 10 February 2023. The linear fit results in $R^2 = 0.94$. A nonlinear quadratic fit results in $R^2 = 0.98$. These fits are only appropriate for the time window and river regions covered by the advection of water parcels described in the text.

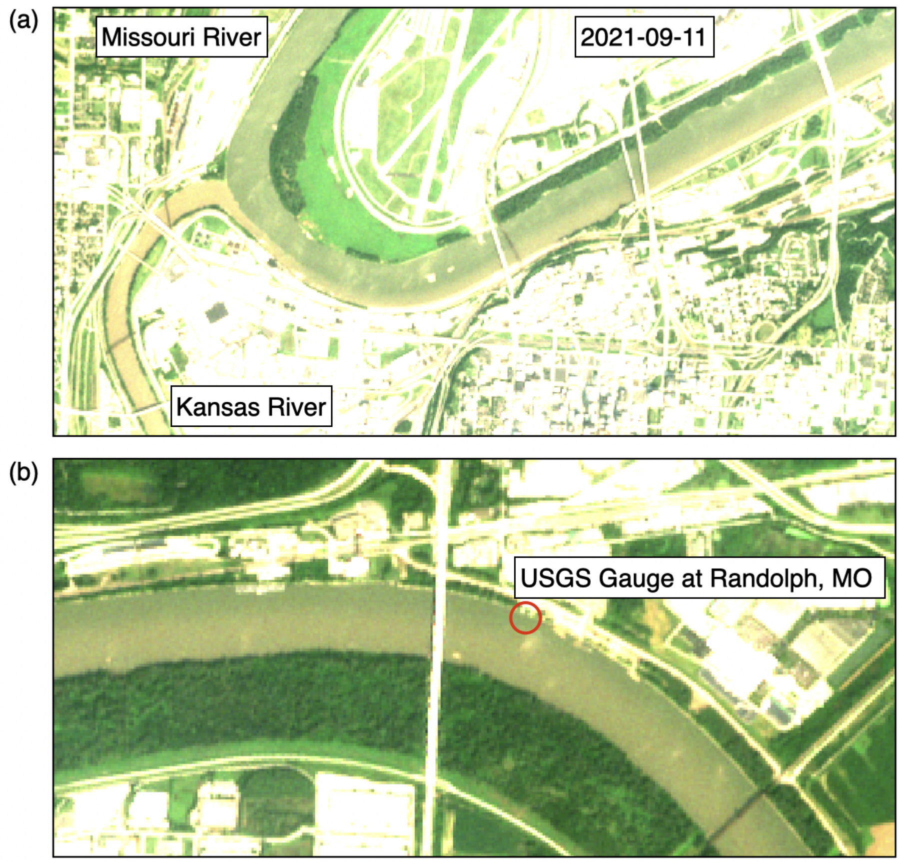

Figure 13: High turbidity Kansas River waters merge and mix with the Missouri River: (a) Sentinel-2 (pseudo) RGB image of the Kansas and Missouri Rivers confluence on 2021-09-11 at 11:22 CST. Water from the Kansas River is concentrated on the south bank of the Missouri River, and (b) higher sediment loads on the south bank are still visible at the USGS station in Randolph, MO, which is seven river miles downstream from the confluence.

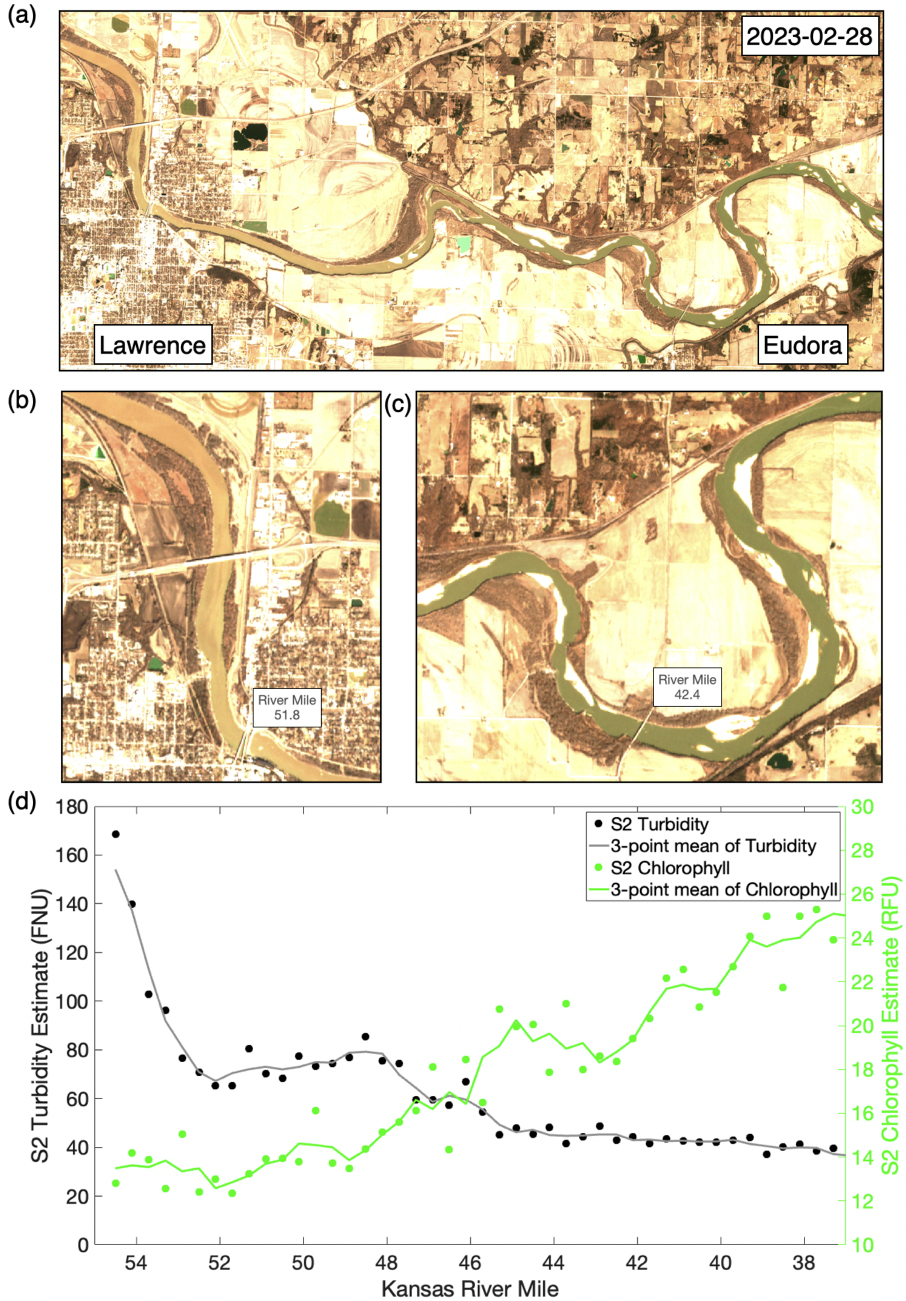

Figure 14: Sentinel-2 images from 28 February 2023 at 11:22 CST show the leading edge of a long turbidity slug that was generated by storm runoff on 27 February 2023 in the Topeka region of Kansas, approximately 30 river miles upstream, (a-c) (pseudo) RGB images showing turbidity gradient, (d) turbidity gradient and chlorophyll-a estimates from Sentinel-2 imagery for points between Lawrence (Bowerstock Dam at River Mile 51.8) and Eudora (Bridge at River Mile 42.4 River Mile).

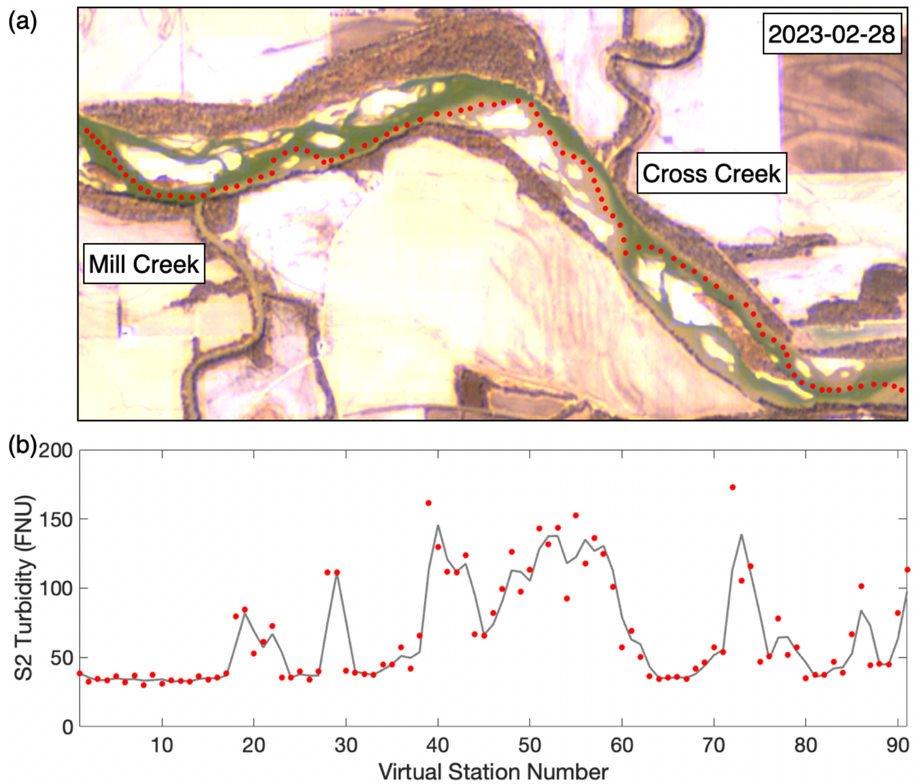

Figure 15: Storm runoff from Mill Creek, west of Topeka, KS, showing inflows with high sediment loads into the Kansas River (a) Sentinel-2 (pseudo) RGB image from 28 February 2023 with the location of 'virtual' gauging stations indicated by red dots (1-91 left to right), (b) Sentinel-2 estimations of turbidity at virtual gauging stations showing sharp changes in turbidity as the path crosses over the interface caused by the sediment loading from Mill Creek and Cross Creek.

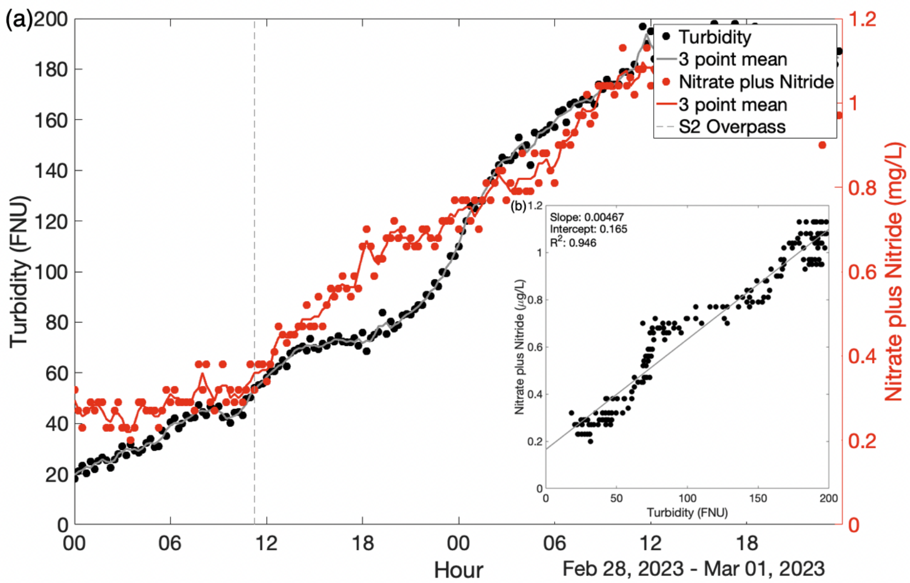

Figure 16: (a) Time series showing the correlation between turbidity and nitrate plus nitrite observed at the USGS station in De Soto, KS, during a 48 hour period from 28 February to 1 March 2023. The correlation is due to the passing of a large slug of turbidity generated by storm runoff upstream east of Topeka, KS (see Fig. 15), (b) Linear fit between nitrate plus nitrite and turbidity results in an $R^2 = 0.946$.

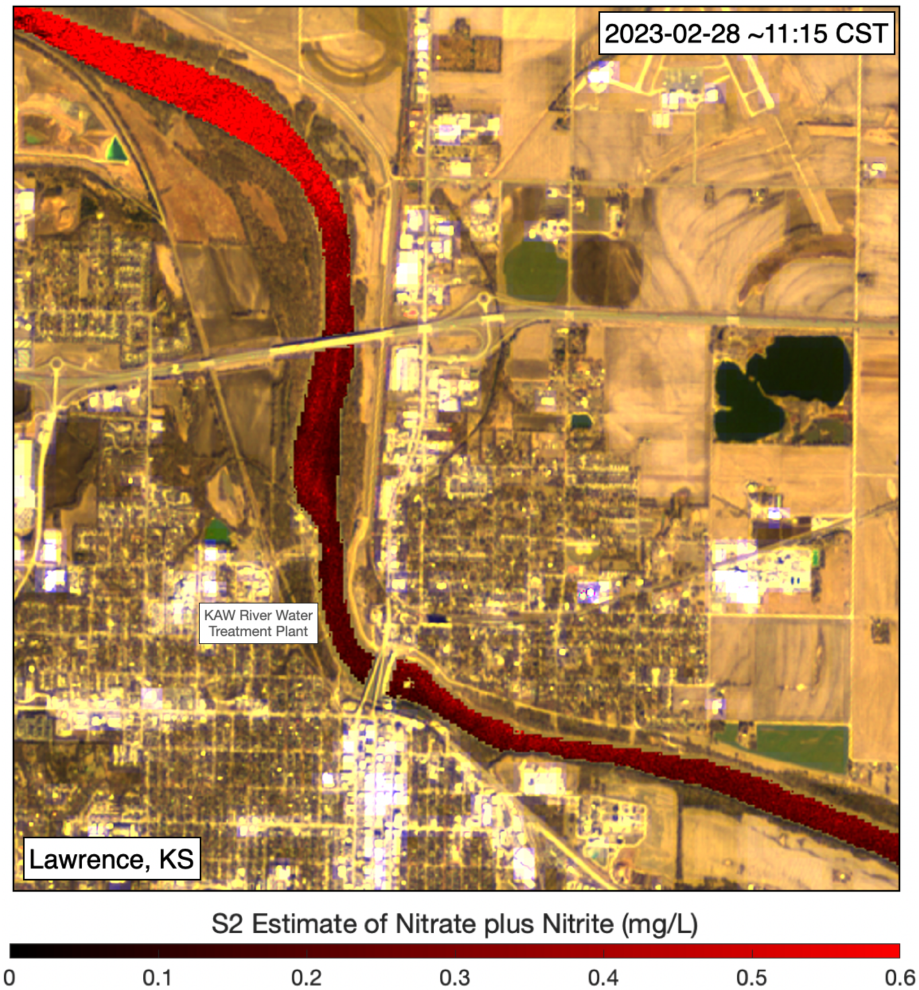

Figure 17: Sentinel-2 estimation of nitrate plus nitrite in the Kansas River on 28 February 2023 at 11:22 CST. The water quality product map was generated with the correlation data described in Fig. 16. The leading edge of the turbidity slug contains elevated levels of nitrate. It is about to pass by the Lawrence drinking water treatment plant with an intake pipe on the West bank of the Kansas River. Water parcels from Lawrence are advected downstream to De Soto (at an estimated rate of 1.6 mph, and travel time of $\sim$13 hr). Hence, the correlations used for the nitrate estimates at Lawrence, KS, contain water parcels that overlap with those used to calibrate the product map. The base map is the Sentinel-2 (pseudo) RGB image from the same day.